Diagn Interv Radiol 2023; DOI: 10.5152/dir.2022.21212

INTERVENTIONAL RADIOLOGY

ORIGINAL ARTICLE

Optimized visualization of focal liver lesions and vascular structures in real-time T1-weighted gradient echo sequences for magnetic resonance-guided liver procedures

Vanessa Franziska Schmidt
Olaf Dietrich
Philipp Maximilian Kazmierczak
Max Seidensticker
Jens Ricke
Marco Armbruster

PURPOSE

This study aimed to determine the optimal sequence parameters of a real-time T1-weighted (T1w) gradient echo (GRE) sequence for magnetic resonance (MR)-guided liver interventions.

METHODS

We included 94 patients who underwent diagnostic liver MR imaging (MRI) and acquired additional real-time T1w GRE sequences with a closed 1.5-T MRI scanner 20 min after a liver-specific contrast agent was injected. In four measurement series, one of the following four sequence parameters was changed, and repeated scans with different values for this parameter were acquired: flip angle (FA) (10–90°), repetition time (TR) (5.47–8.58 ms), bandwidth (BW) (300–700 Hz/pixel), and matrix (96 × 96–256 × 256). Two readers rated the visualizations of the target and risk structures (7-point Likert scale) and the extent of artifacts (6-point Likert scale); they also quantified the lesion–liver contrast ratio, the lesion–liver contrast-to-noise ratio (CNR), and the liver signal-to-noise ratio (SNR). Substratification analyses were performed for differences in overall visual and quantitative assessments depending on the lesion size, type, and the presence of cirrhosis.

RESULTS

For the utilized FAs and matrix sizes, significant differences were found in the visual assessments of the conspicuity of target lesions, risk structures, and the extent of artifacts as well as in the quantitative assessments of lesion–liver contrast ratios and liver SNRs (all $P < 0.001$). No differences were observed for modified TR and BW. Significantly increased conspicuity of the target and vascular structures was observed for both higher FAs and matrix sizes, while the ghosting artifacts increased and decreased, respectively. For primary liver tumors compared with metastatic lesions, and for cirrhotic livers compared with normal liver parenchyma, significantly decreased conspicuity of the target lesions ($P = 0.005$, $P = 0.005$), lesion–liver CNRs ($P = 0.005$, $P = 0.032$), and lesion–liver contrast ratios ($P = 0.015$, $P = 0.032$) were found. All results showed no significant correlation with lesion size.

CONCLUSION

We recommend an FA of 30°–45° and a matrix size of 128 × 128–192 × 192 for MR-guided liver interventions with real-time T1w sequences to provide a balance between good visualizations of target and risk structures, high signal intensities, and low ghosting artifacts. The visualization of the target lesion may vary due to clinical conditions, such as lesion type or associated chronic liver disease.

KEYWORDS

Interventional, lesion-liver CNR, liver SNR, MRI, real-time sequence, sequence parameter, signal intensity, visualization

From the Department of Radiology (V.F.S. ✉ vanessa.schmidt@med.uni-muenchen.de, O.D., P.M.K., M.S., J.R., M.A.), University Hospital, LMU Munich, München, Germany.

Received 18 March 2021; revision requested 19 April 2021; last revision received 13 August 2021; accepted 13 September 2021.

Epub: 05.12.2022

Publication date: 31.01.2023

DOI: 10.5152/dir.2022.21212

Currently, most radiologic interventions are performed using computed tomography, X-ray fluoroscopy, or ultrasound. However, magnetic resonance imaging (MRI) guidance of percutaneous interventions offers numerous advantages for certain procedures, particularly in soft tissue organs like the breast, liver, or prostate.[1-4] This is primarily because the

You may cite this article as: Schmidt VF, Dietrich O, Kazmierczak PM, Seidensticker M, Ricke J, Armbruster M. Optimized visualization of focal liver lesions and vascular structures in real-time T1-weighted gradient echo sequences for magnetic resonance-guided liver procedures. *Diagn Interv Radiol.* 2023;29(1):128-137.

superior soft tissue contrasts in MRIs result in excellent visualizations of target lesions and adjacent structures.[5-7] Therefore, precise needle positioning is supported, and damage to surrounding risk structures that might not have been visualized with other imaging modalities is prevented.[6,8,9] The ability to intra-procedurally monitor thermally induced tissue damage with MR thermometry represents a further benefit of using MR guidance for interventions, particularly for radiofrequency ablation or microwave ablation, and it enables the real-time monitoring of therapy success. Additionally, the real-time multi-planar imaging abilities of fluoroscopic MRI sequences allow the visualization of target lesions and the tracking of instruments in any orientation and in three dimensions; this can be considered an advantage over computerized tomography (CT) guidance, in which pushing the needle outside of the axial planes and working off-plane may be challenging.[10] The lack of ionizing radiation is another key advantage, especially for pediatric patients, women of childbearing age, and repeated or long procedures, and it constitutes a major benefit for treated patients as well as for the medical staff who perform these procedures frequently.[10-12]

Despite these advantages, interventional MRIs are still in the early stages, and CT and ultrasound remain the methods of choice for most percutaneous procedures. However, the introduction of wide-bore MRI systems and real-time high-resolution imaging sequences have significantly improved the acceptance and clinical importance of this technique.[13] Some MR-guided procedures are well established in clinical routines for several indications, e.g., biopsies of breast and prostate lesions,[14,15] while other formats, such as MR-guided procedures in the liver, are continually expanding. In addition to short acquisition times, optimized visualizations of target and risk structures are key to the successful implementation of these procedures.[16-19]

The objective of this prospective monocentric trial was to determine the optimal sequence parameters of a real-time T1-weighted (T1w) gradient echo (GRE) sequence suitable for MR-guided liver interventions with respect to the *in vivo* visualization of focal liver lesions (FLLs), hepatic vascular structures, the extent of ghosting artifacts, and quantitative signal intensities.

Main points

- The results of this study highlight the possibility of optimizing real-time T1-weighted magnetic resonance imaging sequences to achieve appropriate conditions for interventional liver procedures.
- Varied flip angles (FAs) and matrix sizes might affect the conspicuity of target and risk structures, the extent of ghosting artifacts, and signal intensities [lesion–liver contrast-to-noise ratios (CNRs), liver signal-to-noise ratios (SNRs)], while repetition time and bandwidth might be unaffected.
- All results in the visual and quantitative assessments showed no significant correlation with lesion size, while the visualization of the target lesion, lesion–liver CNR, and lesion–liver contrast ratio varied due to clinical conditions, including lesion type and associated chronic liver disease.
- We recommend an FA of 30°–45° and a matrix size of 128 × 128–192 × 192 to provide the optimal balance between a low artifact extent and a good visualization of target lesions and vascular structures in combination with high lesion-liver CNRs and liver SNRs.

Methods

Study design and eligibility criteria

The study was approved by the Local Ethics Committee (application no: 19-976), and informed consent was obtained from each participant. All procedures were performed in accordance with relevant guidelines and regulations according to the Helsinki Declaration of 2013. We included 94 patients with clinical indications who underwent diagnostic MRI examinations of the upper abdomen with weight-based doses of 1.0 mL/10 kg of a liver-specific contrast agent (Gd-EOB-DTPA) (Primovist, Bayer Vital, Leverkusen, Germany). Clinical indications were suspected or known FLL, cirrhosis, or vascular anomalies. Previously treated patients (ablative therapy, liver resection, and/or chemotherapy) and therapy-naive patients were included. During these diagnostic MRIs, additional real-time T1w GRE sequences were acquired within a scan pause immediately prior to the routine measurement of the hepatobiliary phase (20 min after the injection of Gd-EOB-DTPA). Therefore, the overall scan times were not affected by the additionally acquired sequences. The duration of these additional sequences totaled approximately 60 seconds. The exclusion criteria for this study were contraindications against MRI examination or Gd-EOB-DTPA.

The primary endpoint of this study was the visualization of liver lesions and vascular structures in real-time T1w GRE sequences. Secondary endpoints were the extent of visible artifacts as well as the quantitative assessments of lesion–liver contrast ratios, lesion–liver contrast-to-noise ratios (CNRs), and signal-to-noise ratios (SNRs) of the liver parenchyma. In addition, the influence of lesion size in relation to the visual and quantitative assessments was evaluated.

Real-time, T1w MRI sequences at 1.5 T

We performed real-time T1w MRI using a closed whole-body 1.5-T scanner (Magnetom Aera, Siemens Healthineers, Erlangen, Germany) with a short open-bore design (cover-to-cover system length: 145 cm, bore diameter: 70 cm). The gradient system had a maximum gradient strength of 33 mT/m and a slew rate of 125 T/m/s. We acquired four different measurement series, each in axial as well as coronal and sagittal single slices, at the mid hepatic level of the portal vein, via breath-hold acquisitions without acceleration techniques. The slice thicknesses were 10 mm, the fields of view were 360 × 360 mm^2, and the acquisition times were 613–900 ms. In each series, one of the following parameters was systematically and sequentially modified: flip angle (FA), repetition time (TR), bandwidth (BW), and matrix. Each parameter was evaluated in a subgroup of 20 to 30 patients. For each patient, the real-time T1w MRI sequence was repeated with different values per parameter (e.g., FA: 15°, 30°, 45°, 60°), while the other three parameters were held constant. Measurement series 1 was split into two subgroups, with increasing and decreasing values for the varied parameter FAs to evaluate exemplarily the influence of confounding variables, such as the decreasing ability of patients to hold their breath towards the end of the acquisition series. For details on the study design, see Table 1.

Qualitative and quantitative sequence analyses

Image evaluation was performed using Syngo Studio VB36E (Siemens Healthineers, Erlangen, Germany). Two readers with 8 and 2 years' experience in diagnostic liver MRIs independently evaluated the delineations of liver lesions using a Likert-rated scale, as follows: −1= no target lesion within the acquired field of view, 0= lesion not visible, 1= very poor, 2= poor, 3= sufficient, 4= good, and 5= excellent (sharply delineated). The visibility of the vascular structures was graded accordingly from 0 to 5. We employed a rating scale for the visual assessments of the extent of ghosting artifacts, as follows: 0= no

artifacts, 1= very low extent of artifacts, 2= low extent of artifacts, 3= moderate extent of artifacts, 4= strong extent of artifacts, and 5= very strong extent of artifacts.

For the quantitative assessments of the lesion–liver contrast ratios, the lesion–liver CNRs and SNRs of the liver parenchyma in the regions of interest (ROI) of at least 20 mm^2 were used. The ROIs inside the lesions were placed, avoiding areas with hemorrhage or necrosis to prevent susceptibility artifacts. The ROIs within the adjacent liver parenchyma were defined at identical anatomical depths as the lesions to avoid influences of surface coil sensitivity profiles. The sizes and shapes of the ROIs were kept nearly identical for all measurements. Since the intensity of the background noise could not be reliably measured outside the body due to influences of image filters (e.g., intensity normalization and large field-of-view filters),[20,21] we used the standard deviation (SD) of the foreground signal within each ROI to substitute for the noise SD. Then, the SNRs were calculated as the ratios of the foreground signals (the mean value within the ROI) and signal variations (the standard variation within the ROI). The lesion–liver CNRs were determined using the following formula: lesion–liver CNR= (signal intensity$_{liver}$ – signal intensity$_{lesion}$) / sqrt [(SD$_{liver}^2$ + SD$_{lesion}^2$) / 2]. The lesion–liver contrast ratios were defined using the following formula: lesion–liver contrast ratio= signal intensity$_{lesion}$ / signal intensity$_{liver}$.

Statistical analysis

The statistical analysis was performed using SPSS software, version 26 (SPSS Inc., Chicago, Illinois, USA). The visual and quantitative ratings of the two readers were averaged, yielding the primary and secondary efficacy variables for the study. For the descriptive statistics, the numerical values are presented as means plus SD. The Kolmogorov–Smirnov test was used for the assessment of normality. For the k= 24 differences in the conspicuity of the target lesions and vascular structures, artifact behavior, and the quantitative assessments of signal intensities between the modified variables, confirmatory testing was conducted using Friedman's test based on an adjusted significance level of a'= a/k= 0.05/24= 0.00208333, with a Bonferroni correction. All other study testing was performed based on an exploratory significance level of a= 0.05. In the Mann–Whitney U test, substratification analyses were performed for differences in total visual and quantitative assessments (of all measurement series) depending on the presence of cirrhosis and the type of lesion. In addition, the relations between lesion sizes and both assessments were tested using Spearman's rank correlation coefficient.

Results

Patient characteristics

Between January 2020 and May 2020, 94 patients (49 female), with a mean age of 59 years (range: 24–88 years), were included in this study. Liver MRIs were conducted on 91 patients to evaluate known FLLs; thereof, 61/91 patients (67.0%) showed metastatic lesions of various origins (predominantly neuroendocrine and gastrointestinal), 21/91 (23.1%) showed primary liver tumors (hepatocellular carcinoma and cholangiocellular carcinoma), and 5/91 (5.5%) showed benign lesions (liver adenoma/vascular anomaly/liver cyst). In addition, 4/91 (4.4%) patients presented with cirrhosis without any FLL, and 3/91 patients (3.3%) underwent MRIs of the upper abdomen for reasons other than liver pathologies. The FLLs were within the scan range of the fluoroscopic single-slice MRI sequences in 47/91 cases (51.6%), while 44 patients (48.4%) had FLLs outside the acquired scan range. Since we chose a standardized acquisition using a single-slice technique at the level of the hepatic portal vein to achieve the best possible comparability, not all FLLs were included in the datasets. Only one target lesion was chosen randomly for patients with more than one lesion in the image data. These FLLs were primarily metastatic lesions (33/47, 70.2%), followed by hepatocellular carcinomas (6/47, 12.8%), cholangiocellular carcinomas (3/47, 6.4%), liver adenomas (2/47, 4.3%), vascular anomalies (2/47, 4.3%), and liver cysts (1/47, 2.1%). All 94 patients were assessed for the analysis of the visualization of vascular structures and the evaluations of artifact behaviors. In total, 61/91 patients (67.0%) had been treated with previous therapies, of which 35/91 (38.5%) received chemotherapy, 23/91 (25.3%) had liver resections, and 31/91 (38.5%) had local ablative liver procedures. Table 2 lists the additional demographic and clinical characteristics of the patients.

Table 1. Flowchart of study profile. Systematical modification of sequence parameters of real-time T1-weighted gradient-recalled echo sequences of the liver

	Series 1a	Series 1b	Series 2	Series 3	Series 4
	FA (degree)	FA (degree)	TR (ms)	BW (Hz/pixel)	Matrix size
Varied	15 30 45 60	60 45 30 15	5.47 6.25 7.03 7.81 8.58	300 400 500 600 700	96 × 96 128 × 128 192 × 192 256 × 256
Fixed					
FA (°)	Varied	Varied	60	60	60
TR (ms)	4.79	7.03	Varied	7.03	9.4–3.5
BW (Hz/pixel)	795	530	500	Varied	530
Matrix	128 × 128	128 × 128	128 × 128	128 × 128	varied
TE (ms)	2.21	2.5	2.5	3.2	2.5–2.8
FOV	360 × 360	360 × 360	360 × 360	360 × 360	360 × 360
Acquisition time (ms)	613	900	700–1.100	900	900
Slice orientation	cor, ax, sag	cor, ax, sag	cor, ax, sag	cor, ax, sag	cor, ax, sag
Slice thickness (mm)	10	10	10	10	10

FA, flip angle; TR, repetition time; TE, echo time; BW, bandwidth; ms, milliseconds; Hz, Hertz; cor, coronal; ax, axial; sag, sagittal.

Results of measurement series

Sample images of all the modified measurement series are shown in Figures 1–4. Detailed results of the visual and quantitative assessments and the results of Friedman's test are presented in Tables 3 and 4.

Flip angle

There were significant differences for all qualitative and quantitative variables assessed at different FAs (15°–60°) (see Figure 1). Regarding the visualization of the target lesions, the conspicuity of the lesions was significantly different between the selected FAs (P = 0.001). Assessed by the Likert scale, the conspicuity of the lesions showed a mean ± SD score of 1.7 ± 0.3 at FA= 15°, 3.1

± 0.4 at FA= 30°, 3.2 ± 0.7 at FA= 45°, and 3.6 ± 0.8 at FA= 60°. Regarding the visualization of the vascular structures, there were significant differences ($P < 0.001$) in the measurement series, with a Likert-scaled mean ± SD score of 2.0 ± 0.4 at FA= 15°, 3.2 ± 0.6 at FA= 30°, 3.4 ± 0.5 at FA= 45°, and 3.8 ± 0.5 at FA= 60°. Significant differences occurred in the extent of ghosting artifacts between the individual FAs, with more severe artifacts occurring for higher FAs, with a mean ± SD score of 1.0 ± 0.4 at FA= 15°, 1.8 ± 0.5 at FA= 30°, 2.9 ± 0.6 at FA= 45°, and 3.2 ± 0.8 at FA= 60°.

Similar results were found for the quantitative assessments of signal intensities; the lesion–liver contrast ratios and the liver SNRs presented with significant differences between the selected FAs ($P < 0.001$, $P < 0.001$). The lowest value of the lesion–liver contrast ratio corresponding to the highest difference of signal intensities between lesion and liver parenchyma was found with a mean ± SD score of 0.4 ± 0.2 for medium and high FAs of 30°, 45°, and 60°, respectively. Conversely, high lesion–liver CNRs were shown for the FAs of 15°, 45°, and 60°, with a mean ± SD score of 8.4 ± 4.6, 8.8 ± 3.2, and 8.9 ± 3.9, respectively. The highest liver SNR with a mean ± SD score of 16.9 ± 6.8 was revealed for FA= 15°.

Repetition time

There were no significant differences in the assessed qualitative and quantitative variables for different TRs (5.47–8.58 ms); the conspicuity of the target lesions ($P = 0.14$), the vascular structures ($P = 0.51$), the artifact extents ($P = 0.53$), the lesion–liver contrast ratios ($P = 0.42$), the lesion–liver CNRs ($P = 0.22$), and the liver SNRs ($P = 0.31$) were not dependent on the different selected TRs (see Figure 2).

Table 2. Patient and clinical characteristics of the study cohort (n = 94)

Characteristics	n (%)
Sex	
Male	45 (47.9%)
Female	49 (52.1%)
Age (years), mean ± SD	59 ± 17
Liver disease	91 (96.8%)
CCA	6 (6.4%)
HCC	15 (16.0%)
Metastasis	61 (64.9%)
BC	4 (4.3%)
CRC	10 (10.6%)
GCT	1 (1.1%)
LMS	2 (2.1%)
MM	4 (4.3%)
NET	33 (35.1%)
NSCLC	1 (1.1%)
PC	1 (1.1%)
STS	1 (1.1%)
TC	2 (2.1%)
UC	2 (2.1%)
Liver adenoma	2 (2.1%)
Liver cyst	1 (1.1%)
Vascular anomaly	2 (2.1%)
Cirrhosis	4 (4.3%)
No liver disease	3 (3.2%)
Previous therapies	61 (64.9%)
Chemotherapy	35 (37.2%)
Liver resection	23 (24.5%)
Ablative therapy	31 (33.0%)
FLL size (mm), mean ± SD	38.8 ± 20.0

BC, breast cancer; CCA, cholangiocarcinoma; HCC, hepatocellular carcinoma; CRC, colorectal cancer; GCT, germ-cell tumor; LMS, leiomyosarcoma; MM, malignant melanoma; NSCLC, non-small cell lung carcinoma; PC, pancreatic cancer; STS, soft tissue sarcoma; TC, thyroid cancer; UC, urothelial cancer; FLL, focal liver lesion; SD, standard deviation.

Bandwidth

There were no significant differences for the assessed qualitative and quantitative variables for different BWs (300–700 Hz/pixel); the conspicuity of the target lesions ($P = 0.85$), the vascular structures ($P = 0.87$), the artifact extents ($P = 0.80$), the lesion–liver contrast ratios ($P = 0.11$), the lesion–liver CNRs ($P = 0.44$), and the liver SNRs ($P = 0.26$) were not dependent on different selected BWs (see Figure 3).

Matrix

There were significant differences for all qualitative and quantitative variables assessed at different matrix sizes (96 × 96–256 × 256) (see Figure 4). Regarding the visualizations of target lesions, there was better conspicuity of the lesions for larger matrix sizes ($P < 0.001$). The conspicuity of the target lesions showed a mean ± SD score of 1.8 ± 0.6 at 96 × 96, 2.7 ± 0.5 at 128 × 128, 3.5 ± 0.5 at 192 × 192, and 3.8 ± 0.6 at 256 × 256. In the visual assessments of the vascular structures, there was a better delimitation of structures with larger matrices ($P < 0.001$). Rated by a Likert scale, the series of the vascular structure yielded a mean ± SD score of 2.0 ± 0.2 at 96 × 96, 3.0 ± 0.3 at 128 × 128, 3.7 ± 0.5 at 192 × 192, and 4.2 ± 0.6 at 256 × 256. There was a significantly different extent of ghosting artifacts depending on the chosen matrix size ($P < 0.001$), with fewer artifacts for larger matrices, with a mean ± SD score of 3.5 ± 0.5 at 96 × 96, 2.4 ± 0.5 at 128 × 128, 1.4 ± 0.5 at 192 × 192, and 0.7 ± 0.8 at 256 × 256 (see Figure 5).

The following results were found for the quantitative assessments of signal intensities: the liver SNR presented with significant differences between the selected matrix sizes ($P < 0.001$), but the highest value of the lesion–liver contrast ratio corresponding to the lowest difference of signal intensities between lesions and the liver parenchyma was found with a mean ± SD score of 0.5 ± 0.3 for low matrix sizes of 96 × 96. The highest lesion–liver CNR, with a mean ± SD score of 9.7 ± 6.1, and liver SNR, with a mean ± SD score of 15.9 ± 6.2, were shown at 96 × 96 (see Figure 6).

Impact of type of lesion, liver cirrhosis, and lesion size

Regarding the total visual and quantitative assessments, compared with patients with primary liver tumors (n = 10), the group with metastatic lesions (n = 33) presented with significantly higher mean conspicuity of the target lesions (P = 0.005) as well as significantly increased mean lesion–liver CNRs (P = 0.005) and lesion–liver contrast ratios (P = 0.015). No significant differences were seen in the conspicuity of the vascular structures (P = 0.96), the artifact extents (P = 0.28), or the liver SNRs (P = 0.98). Compared with the group with normal liver parenchyma (n = 41), the patients with cirrhotic liver disease (n = 6) revealed significantly decreased mean conspicuity of the target lesions (P = 0.005) as well as significantly decreased mean lesion–liver CNRs (P = 0.032) and lesion–liver contrast ratios (P = 0.032). No significant differences were observed in the conspicuity of vascular structures (P = 0.45), artifact extents (P = 0.16), or liver SNRs (P = 0.74). The detailed results are presented in Tables 5 and 6. The mean (± SD) size of the evaluated FLLs was 38.8 mm (± 20.0 mm). The results of the visual and quantitative assessments showed no significant correlations with lesion size (all P > 0.84).

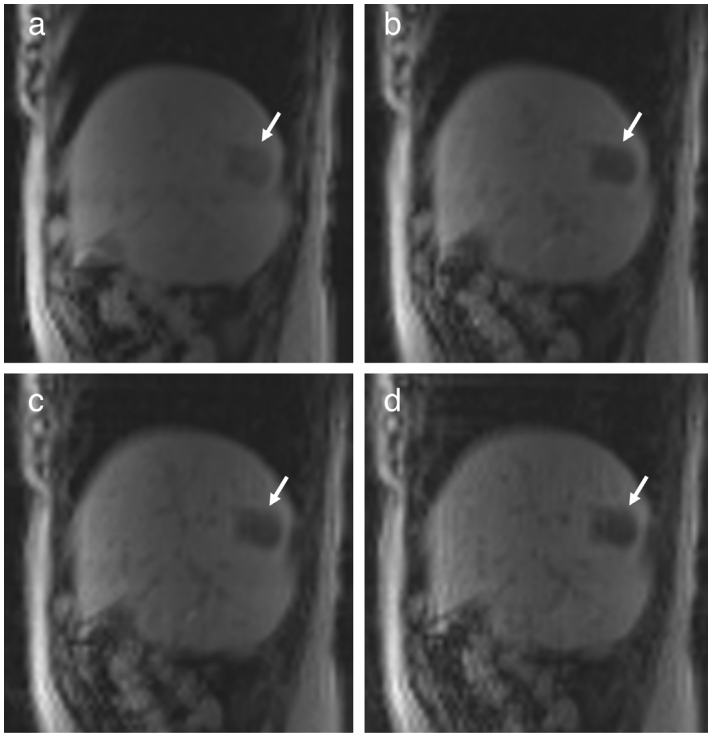

Figure 1. Measurement series **(a, b)**. Real-time T1-weighted gradient-recalled echo sequences showing sagittal planes with different flip angles performed in increasing order (measurement series 1a), 15°, 30°, 45°, and 60° **(a-d)**. Note the different conspicuity of the hypointense target lesion (arrows) and vascular structures and the different extent of artifacts. Measurement series 1b in decreasing order (60°, 45°, 30°, and 15°) showed similar results.

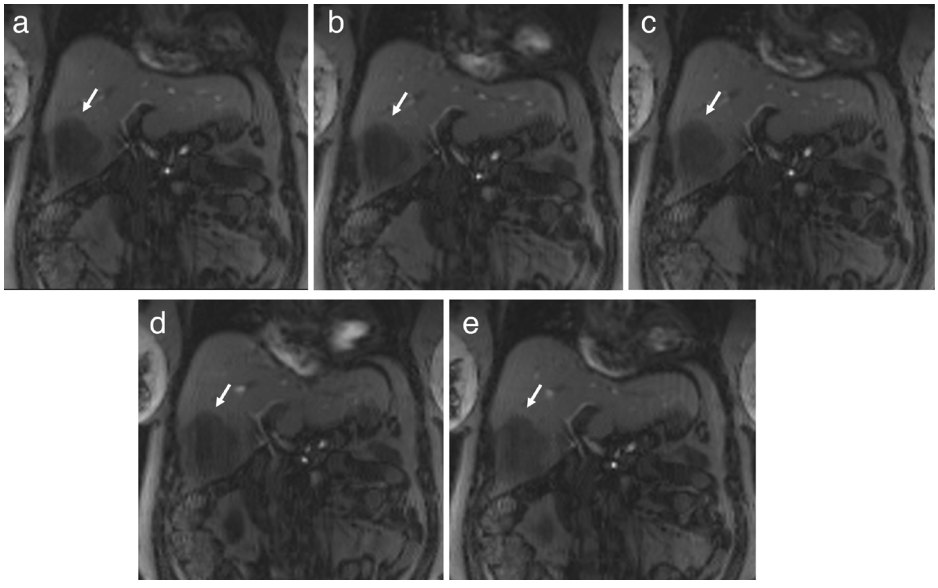

Figure 2. Measurement series 2. Real-time T1-weighted gradient-recalled echo sequences showing coronal planes with different repetition times of 5.47, 6.25, 7.03, 7.81, and 8.59 ms **(a-e)**. Note the absence of difference in the conspicuity of hypointense target lesion (arrows) and vascular structures and the similar extent of artifacts.

Discussion

Concerning MR-guided liver interventions, the purpose of this study was to determine the optimal sequence parameters of a real-time T1w GRE sequence, which was acquired 20 min after the injection of a liver-specific contrast agent. In the literature, various real-time sequences have been evaluated for image-guided procedures of the liver, exemplarily by Rempp et al.[17] They assessed the conspicuity of FLL with a non-contrast T1w spoiled GRE sequence as well as a predominantly T2w balanced steady-state free precession sequence, revealing that 20% of hepatic lesions could not be detected through the use of these sequences. Consequently, the use of liver-specific contrast agents may be beneficial in interventional settings, comparable to diagnostic MRIs, in which contrast-enhanced T1w sequences constitute the current reference standard to detect and characterize FLLs.[22]

In this systematic evaluation of sequence parameters, significant differences were found for the visual assessments of the target and risk structures and the extent of artifacts as well as for the quantitative assessment of signal intensities depending on the used FA and matrix size. No differences were found for TR and BW.

Regarding the FA, better conspicuity of the lesions and vascular structures was observed for higher FAs, with better results for 30° compared with 15°, while there were only minor differences between 30° and 60°. This is in contrast to contrast-enhanced MRI using the T1w GRE sequence for diagnostic purposes, in which the FA usually ranges from 10° to 15°.[23]

Another aspect to consider is the decrease in SNR with increasing FA above the Ernst angle (α_E) in fluoroscopic GRE sequences. It is known that the MR signal is maximized at α_E,

which can be calculated from the equation α_E= arccos [exp(−TR/T1)][24] As exemplarily presented in previous work by Nagle et al.[25], this equation leads to the highest liver SNR at 20°–35° in diagnostic hepatocyte phase imaging. In our study, the α_E was lower in combination with a short TR (4.79–7.03 ms) in the fluoroscopic GRE sequences, so high and medium FAs did not lead to optimal liver SNRs. However, for MR interventions, and with respect to target conspicuity, the lesion–liver CNR, which was maximized at 30° and 45° in our assessment, can be considered more important than the SNR of the liver parenchyma in the setting of MR interventions. Increasing the FA in the hepatocyte phase reduces the SNR of non-hepatocyte-containing tissues, e.g., of FLL, without an effective transport mechanism, resulting in an improved lesion–liver CNR with the highest values at 30°–45°. Due to higher SD_{liver} and SD_{lesion} at 60°, the CNR is lower again at these FAs, while the lesion–liver contrast ratio is similarly high at 60°, compared with that at 30° and 40°. These contrast ratios are the consequence of increasing T1 weighting, causing greater differences in contrast agent loads and thus optimizing the image contrasts between the FLL and the surrounding liver parenchyma.[23] However, a theoretical calculation is difficult and might not be feasible due to the unknown T1 values of the different FLLs, which are necessary for the calculation. In measurement series 1 of this study, more severe artifacts occurred for higher FAs (see Figure 1) in both increasing and decreasing measurement orders, indicating that this was a true effect; it was not confounded by the acquisition of higher FA measurements later during the scan and might have been affected by strong breathing artifacts. More precisely, we evaluated large differences in artifact extent between 15° and 30° and between 30° and 45°, while there were only slight differences between 45° and 60°. This is in line with the results of previous work. Exemplarily, Epstein et. al.[26] evaluated RF-spoiled GRE sequences in a phantom study and compared FAs from 10° to 40°, resulting in more severe artifacts with an increased FA of 40°.

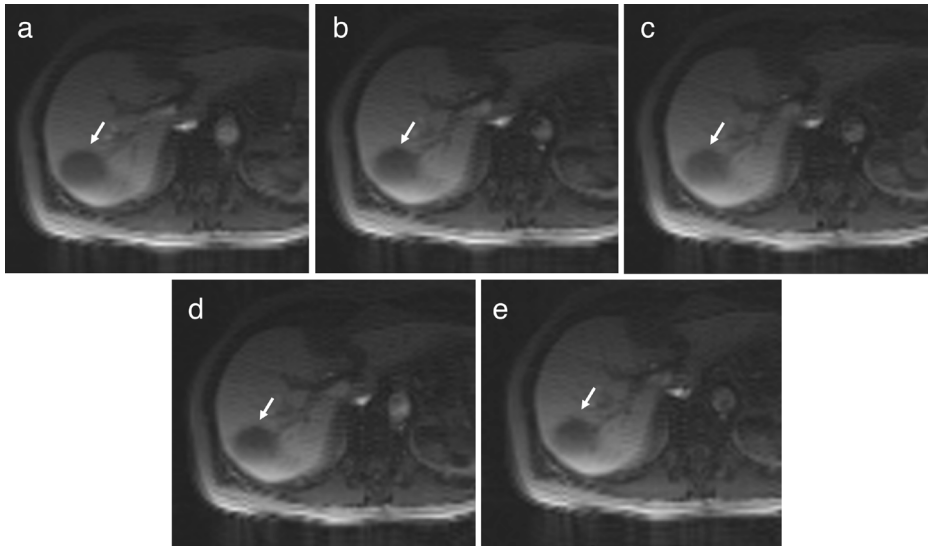

Figure 3. Measurement series 3. Real-time T1-weighted gradient-recalled echo sequences showing axial planes with different bandwidths of 300, 400, 500, 600, and 700 Hz/pixel **(a-e)**. Note the absent difference in conspicuity of hypointense target lesion and vascular structures and the similar extent of artifacts.

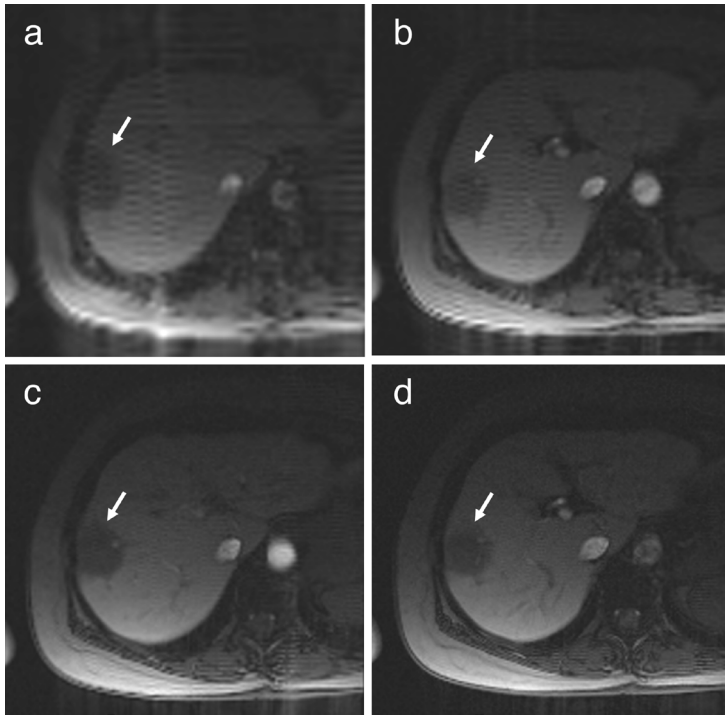

Figure 4. Measurement series 4. Real-time T1-weighted gradient-recalled echo sequences showing axial planes with different matrix sizes: 96 × 96, 128 × 128, 192 × 192, and 256 × 256 **(a-d)**. Note the difference in the conspicuity of hypointense target lesion (arrows) and vascular structures and the different extent of artifacts.

Regarding the matrix, there was better conspicuity of the target lesions and vascular structures as the matrix was increased. The greatest difference in the visual and quantitative assessments of the target lesions and vascular structures was found between 128 × 128 and 192 × 192. However, this difference in the conspicuity of the FLLs and vascular structures between the two matrix sizes is less than the difference between FAs of 15° and 30°. The chosen matrix size determines the voxel size, and thus, the spatial resolution; therefore, it is a quality feature of the acquired image data.[27] Thus, it is reasonable that a lower matrix size leads to worse conspicuity of target lesions and vascular structures due to an increased blurring of the images. On the other hand, the quantitative assessments of signal intensities showed significantly higher liver SNRs with decreasing matrix sizes. Thereby, the lesion–liver CNR also demonstrated increases; however, in comparison with the FA measurement series, these differences were not significant, as potentially may be expected with a larger sample size. Previous work has already revealed the effect of matrix and voxel size on signal intensities, concurring with our findings.[28] Our results suggest that for the visualization of target and risk structures in fluoroscopy images, spatial resolution and image quality have more impact than the corresponding differences in signal intensities.

Regarding the extent of ghosting artifacts, fewer artifacts occurred as the matrix sizes increased. More precisely, we evaluated

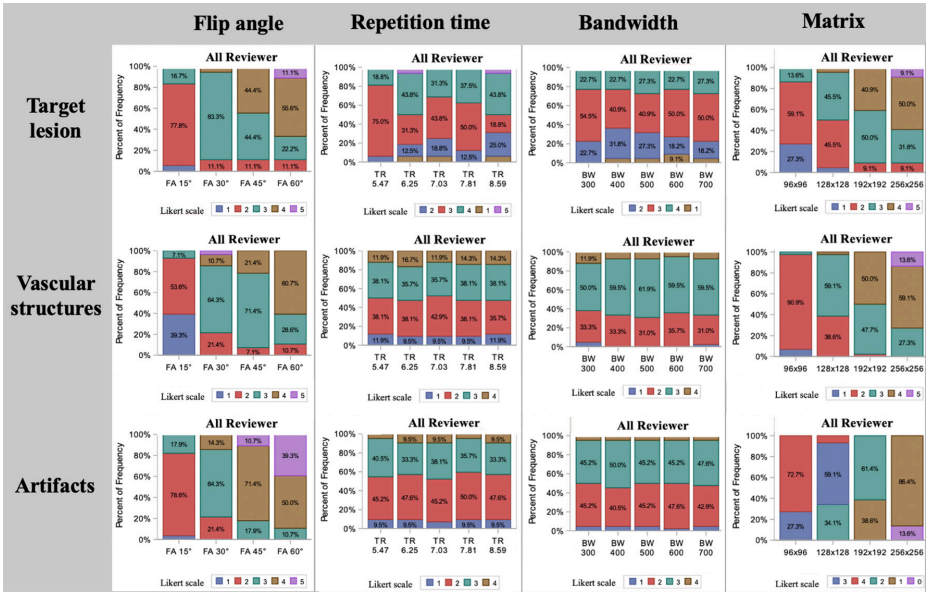

Figure 5. Results of visual assessment. Stacked column chart of measurement results of both readers (first row, conspicuity of target lesion; second row, conspicuity of vascular structures; third row, extent of artifacts) relative to the varied sequence parameters flip angle (first column, 15°–60°), repetition time (second column, 5.47–8.59 ms), bandwidth (third column, 300–700 Hz/pixel), and matrix size (fourth column, 96 × 96–256 × 256).

Table 3. Visual assessment for modified sequence parameters of T1-weighted gradient-recalled echo fluoroscopy images by two independent readers. Qualitative data assessment in the use of a Likert scale for the visualization of the target lesion and vascular structures (−1 to 5), artifact behavior (0 to 5), and corresponding Friedman's test results. Values of both readers were averaged and are presented as means ± standard deviation

	Target lesion *P* value	Vascular structures *P* value	Artifacts *P* value
FA (n = 30)	*P* = 0.001*	*P* < 0.001*	*P* < 0.001*
15	1.7 ± 0.3	2.0 ± 0.4	1.1 ± 0.6
30	3.1 ± 0.4	3.2 ± 0.6	1.9 ± 0.5
40	3.2 ± 0.7	3.4 ± 0.5	3.0 ± 0.6
60	3.6 ± 0.8	3.8 ± 0.5	3.5 ± 0.7
TR (n = 21)	*P* = 0.14	*P* = 0.51	*P* = 0.53
5.46	3.1 ± 0.4	2.6 ± 0.9	2.6 ± 0.9
6.25	2.5 ± 1.2	2.7 ± 0.8	2.6 ± 0.9
7.03	2.9 ± 1.1	2.6 ± 0.8	2.6 ± 0.9
7.81	3.4 ± 0.7	2.8 ± 0.9	2.4 ± 0.9
8.58	3.4 ± 1.3	2.7 ± 0.9	2.6 ± 0.9
BW (n = 21)	*P* = 0.85	*P* = 0.87	*P* = 0.80
300	3.1 ± 0.5	2.6 ± 0.5	2.3 ± 0.7
400	2.9 ± 0.7	2.7 ± 0.5	2.4 ± 0.7
500	3.1 ± 0.7	2.7 ± 0.5	2.3 ± 0.7
600	3.0 ± 0.9	2.6 ± 0.5	2.4 ± 0.6
700	3.1 ± 0.9	2.7 ± 0.5	2.4 ± 0.7
Matrix (n = 22)	*P* < 0.001*	*P* < 0.001*	*P* < 0.001*
96 × 96	1.8 ± 0.6	2.0 ± 0.2	3.5 ± 0.5
128 × 128	2.7 ± 0.5	3.0 ± 0.3	2.4 ± 0.5
192 × 192	3.5 ± 0.5	3.7 ± 0.5	1.4 ± 0.5
256 × 256	3.8 ± 0.6	4.2 ± 0.6	0.7 ± 0.5

*Statistical significance was considered at P < 0.0021 using a Bonferroni correction. FA, flip angle (degree); TR, repetition time (ms); BW, bandwidth (Hz/pixel); SD, standard deviation.

differences in artifact extent proportional to the matrix size (see Figure 4). The advantages of a higher matrix size are offset–besides by decreasing the SNR and CNR–by a longer acquisition time, resulting in a worse temporal resolution, which is crucial for guidance control and safety during interventions. Consequently, as a compromise, a medium matrix size proves to be optimal.

Regarding the chosen BW, our findings showed no differences in the visual assessments of the target and risk structures and the extent of artifacts or in the quantitative assessments of signal intensities. Contingently, the evaluated range was too small, although it was selected to clinical standards. It is well known that a higher BW enables faster data acquisition and minimizes chemical shift artifacts, but it also reduces SNR, as more noise is included. In addition, the chosen BW alters the extent of susceptibility artifacts, which are particularly important for needle interventions.[27] In summary, our study also suggests high BW values that are preferable to reduce metal artifacts while not significantly decreasing image quality. Regarding the TR, no significant differences in visual and quantitative assessments were found, which is of interest, as lower TRs result in shorter acquisition times, with consequently shorter image refresh rates during MR fluoroscopy.

Furthermore, our evaluation of the total visual and quantitative assessments revealed increased target visualizations and higher lesion–liver CNRs and contrast ratios of metastatic lesions in comparison with primary liver tumors. This is in line with the results of previous studies. Okada et al.[29] reported decreased visual conspicuity and signal intensities for hepatocellular carcinomas, compared with metastatic lesions, during FA modification using a contrast-enhanced T1w MRI protocol. In addition, when comparing cirrhotic with normal liver parenchyma, we found decreased target visualizations and decreased lesion–liver CNRs and contrast ratios in the event of chronic liver disease. This may be due to the circumstance of decreased contrast agent uptake of hepatocytes in cirrhotic liver parenchyma. Consequently, cirrhotic liver parenchyma may show reduced enhancement in the hepatobiliary phase, resulting in decreased lesion–liver contrast.[30,31] All the results of the visual and quantitative assessments showed no significant correlations to lesion size, similar to the findings of Rempp et al.[17] Accordingly, the individual clinical conditions of patients may have more impact on

the conspicuity of FLLs during MR-guided procedures than lesion sizes.

The present study has certain limitations. Some of the included patients had no FLLs, and additionally, not all FLLs were included in the datasets of the acquired scan range because of the standardized acquisition by the single-slice technique at the level of the hepatic portal vein. Furthermore, a part of the cohort had received previous therapy (partial liver resection and/or local ablation), which may have led to anatomical distortion and impacted the visualization of target and risk structures compared with the situation in therapy-naive patients. However, this heterogeneous cohort with both pre-treated and therapy-naive patients may illustrate a realistic view of MR-guided liver procedures, which are performed mainly in patients suffering from oncologic diseases, where there is a need for multimodal therapy concepts. Imaging was performed with just one MR scanner with 1.5-T field strength, and the influence of different magnetic field strengths was not considered. In addition, the measurement series was performed during routine imaging in diagnostic settings and not under interventional conditions. Consequently, there may be additional factors that influence the visualization of target and risk structures during interventional procedures that may hamper the direct extrapolation of our results. Finally, MR-guided interventions do not require only sequences adapted for the optimal visualization of target and vascular structures; the sequences also must be adapted to interventional instruments to minimize the extent of susceptibility artifacts. Thus, the analysis of susceptibility artifacts for different interventional needles using the optimized and specified sequences should be the subject of future studies.

Concerning the clinical practice and further developments of interventional MRIs of the liver, e.g., for biopsies, microwave ablations, percutaneous transhepatic cholangiodrainage, radiofrequency ablations, or brachytherapy, the results of this study highlight the possibility of optimizing real-time T1w MRI sequences to achieve appropriate conditions for interventional procedures.

In conclusion, we recommend an FA of 30°–45° and a matrix size of 128 × 128–192 × 192 to provide the optimal balance between a low extent of artifacts and a good visualization of target lesions and vascular structures in combination with high lesion–liver CNRs and liver SNRs. The visualization of the target lesion may vary due to clinical conditions, such as lesion type or associated chronic liver disease.

Table 4. Quantitative assessment of lesion–liver contrast ratio (0 to 1), lesion–liver contrast-to-noise ratio, and liver signal-to-noise ratio for modified sequence parameters of T1-weighted gradient-recalled echo fluoroscopy images and the corresponding Friedman's test results. Values of both readers were averaged and are represented as means ± standard deviation

Mean lesion size (mm)		Mean lesion–liver CNR *P* value	Mean SNR liver *P* value	Mean lesion–liver contrast ratio *P* value
FA (n = 30)	40.4 ± 18.2	*P* = 0.004	*P* < 0.001*	*P* < 0.001*
15		8.4 ± 4.6	16.9 ± 6.8	0.6 ± 0.2
30		8.8 ± 3.2	13.5 ± 4.5	0.4 ± 0.2
45		8.9 ± 3.9	12.2 ± 4.4	0.4 ± 0.2
60		7.0 ± 3.1	10.1 ± 3.9	0.4 ± 0.2
TR (n = 21)	32.5 ± 22.4	*P* = 0.22	*P* = 0.31	*P* = 0.42
5.46		8.5 ± 4.9	13.9 ± 5.0	0.5 ± 0.3
6.25		7.8 ± 4.2	12.7 ± 4.3	0.5 ± 0.3
7.03		9.2 ± 4.8	13.5 ± 5.1	0.5 ± 0.2
7.81		8.8 ± 4.5	13.8 ± 6.1	0.5 ± 0.3
8.58		8.5 ± 4.7	13.9 ± 6.3	0.5 ± 0.2
BW (n = 21)	38.3 ± 18.0	*P* = 0.44	*P* = 0.26	*P* = 0.11
300		8.5 ± 3.6	13.6 ± 4.3	0.4 ± 0.1
400		9.1 ± 4.2	14.5 ± 7.1	0.4 ± 0.2
500		8.2 ± 4.4	13.2 ± 5.3	0.4 ± 0.1
600		9.2 ± 4.4	15.0 ± 6.3	0.4 ± 0.1
700		9.1 ± 4.7	13.8 ± 5.7	0.4 ± 0.2
Matrix (n = 20)	42.6 ± 23.1	*P* = 0.037	*P* < 0.001*	*P* = 0.008
96 × 96		9.7 ± 6.1	15.9 ± 6.2	0.5 ± 0.3
128 × 128		9.4 ± 5.1	13.4 ± 3.5	0.4 ± 0.2
192 × 192		8.3 ± 4.5	11.6 ± 2.5	0.4 ± 0.2
256 × 256		7.5 ± 4.0	10.2 ± 2.7	0.4 ± 0.2

*Statistical significance was considered at *P* < 0.0021 using a Bonferroni correction. FA, flip angle (degree); TR, repetition time (ms); BW, bandwidth (Hz/pixel); CNR, contrast-to-noise ratio; SNR, signal-to-noise ratio.

Table 5. Substratification analyses. The results of a Mann–Whitney U test between the group with metastatic lesions (n = 33) and patients with primary liver tumors (n = 10) present significant differences in the visual assessment of the target lesion and in the lesion–liver contrast-to-noise ratios and lesion–liver region-of-interest ratios. Values are presented as medians (interquartile range)

Total assessment	Primary liver tumor (n = 10)	Metastatic lesion (n = 33)	*P* value
Target lesions	3.0 (2.0–3.0)	3.0 (3.0–4.0)	*P* = 0.005*
Vascular structures	3.0 (2.0–3.0)	3.0 (2.0–3.0)	*P* = 0.96
Artifacts	3.0 (2.0–3.0)	2.0 (2.0–3.0)	*P* = 0.28
Lesion–liver ROI ratio	0.4 (0.3– 0.6)	0.3 (0.2–0.5)	*P* = 0.015*
Liver SNR	13.0 (9.5–16.2)	13.1 (10.2–19.6)	*P* = 0.98
Lesion–liver CNR	7.7 (5.6–10.8)	10.0 (7.2–13.5)	*P* = 0.005*

*Statistical significance was considered at *P* < 0.05. ROI, region of interest; SNR, signal-to-noise ratio; CNR, contrast-to-noise ratio.

Conflict of interest disclosure

The authors declared no conflicts of interest.

Table 6. Substratification analyses. The results of a Mann–Whitney U test between the group with cirrhotic liver parenchyma (n = 6) and patients with normal liver parenchyma (n = 41) present significant differences in the visual assessment of the target lesion and in the lesion–liver contrast-to-noise ratio and lesion–liver region-of-interest ratio. Values are presented as medians (interquartile range)

Total assessment	Liver cirrhosis (n = 6)	Normal liver parenchyma (n = 41)	*P* value
Target lesion	2.0 (2.0–3.0)	3.0 (3.0–4.0)	*P* = 0.005*
Vascular structures	3.0 (2.0–3.0)	3.0 (2.0–3.0)	*P* = 0.45
Artifacts	3.0 (2.0–3.0)	2.0 (2.0–3.0)	*P* = 0.16
Lesion–liver ROI ratio	0.4 (0.3–0.6)	0.3 (0.2–0.5)	*P* = 0.032*
Liver SNR	12.1 (9.0–16.3)	13.0 (9.5–15.9)	*P* = 0.74
Lesion–liver CNR	7.6 (5.0–11.0)	9.7 (6.8–13.3)	*P* = 0.032*

*Statistical significance was considered at $P < 0.05$. ROI, region of interest; SNR, signal-to-noise ratio; CNR, contrast-to-noise ratio.

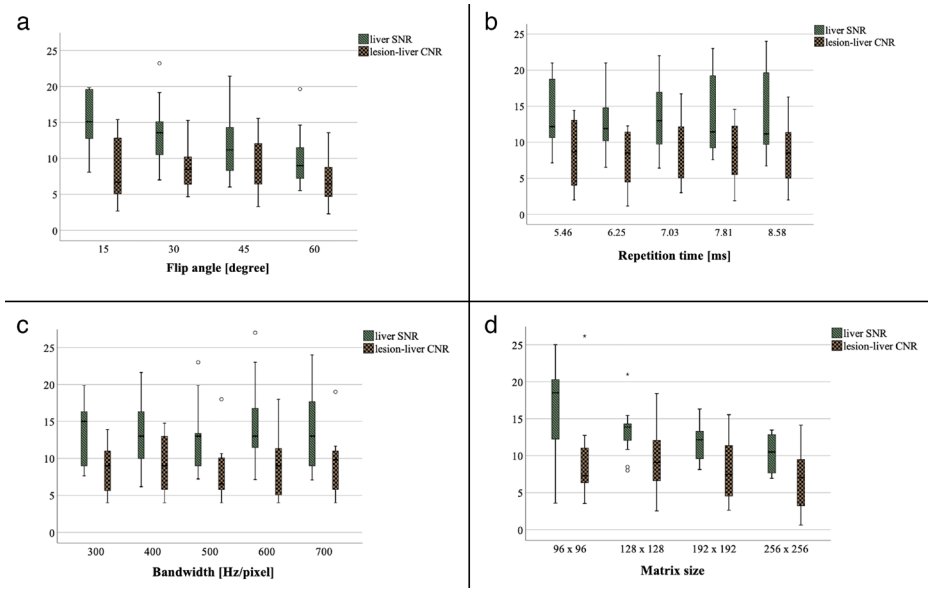

Figure 6. Results of qualitative assessment. Box and whisker plots of the lesion–liver contrast-to-noise ratio (CNR) and the liver signal-to-noise ratio (SNR) for the modified sequence parameters of T1-weighted gradient-recalled echo fluoroscopy images **(a-d)**. The upper and lower ends of the vertical lines show the upper and lower extremes, respectively. The upper and lower margins of the boxes show the upper and lower quartiles, respectively. The horizontal lines in the boxes show the medians. Note the dependence of signal on the flip angle, with significantly higher liver SNR at 15° and lesion–liver CNR at 30°–60° **(a)**. The SNR of the liver parenchyma and the lesion–liver CNR significantly decreases with higher matrix sizes **(d)**.

References

1. Winkelmann MT, Gohla G, Kubler J, et al. MR-guided high-power microwave ablation in hepatic malignancies: initial results in clinical routine. *Cardiovasc Intervent Radiol*. 2020;43(11):1631-1638. [CrossRef]
2. Elfatairy KK, Filson CP, Sanda MG, Osunkoya AO, Nour SG. In-Bore MRI-guided prostate biopsies in patients with prior positive transrectal US-guided biopsy results: pathologic outcomes and predictors of missed cancers. *Radiol Imaging Cancer*. 2020;2(5):e190078. [CrossRef]
3. Winkelmann MT, Archid R, Gohla G, et al. MRI-guided percutaneous thermoablation in combination with hepatic resection as parenchyma-sparing approach in patients with primary and secondary hepatic malignancies: single center long-term experience. *Cancer Imaging*. 2020;20(1):37. [CrossRef]
4. Weiss J, Hoffmann R, Rempp H, et al. Feasibility, efficacy, and safety of percutaneous MR-guided ablation of small (</=12 mm) hepatic malignancies. *J Magn Reson Imaging*. 2019;49(2):374-381. [CrossRef]
5. Fischbach F, Thormann M, Seidensticker M, Kropf S, Pech M, Ricke J. Assessment of fast dynamic imaging and the use of Gd-EOB-DTPA for MR-guided liver interventions. *J Magn Reson Imaging*. 2011;34(4):874-879. [CrossRef]
6. Fischbach F, Bunke J, Thormann M, et al. MR-guided freehand biopsy of liver lesions with fast continuous imaging using a 1.0-T open MRI scanner: experience in 50 patients. *Cardiovasc Intervent Radiol*. 2011;34(1):188-192. [CrossRef]
7. Donato H, França M, Candelária I, Caseiro-Alves F. Liver MRI: from basic protocol to advanced techniques. *Eur J Radiol*. 2017;93:30-39. [CrossRef]
8. Bock M, Umathum R, Zuehlsdorff S, et al. Interventional magnetic resonance imaging: an alternative to image guidance with ionising radiation. *Radiat Prot Dosimetry*. 2005;117(1-3):74-78. [CrossRef]
9. Weiss J, Hoffmann R, Clasen S. MR-guided liver interventions. *Top Magn Reson Imaging*. 2018;27(3):163-170. [CrossRef]
10. Barkhausen J, Kahn T, Krombach GA, et al. White paper: interventional MRI: current status and potential for development considering economic perspectives, part 1: general application. *Rofo*. 2017;189(7):611-623. [CrossRef]
11. Ricke J, Thormann M, Ludewig M, et al. MR-guided liver tumor ablation employing open high-field 1.0T MRI for image-guided brachytherapy. *Eur Radiol*. 2010;20(8):1985-1993. [CrossRef]
12. Fischbach F, Fischbach K, Ricke J. Percutaneous interventions in an open MR system: technical background and clinical indications. *Radiologe*. 2013;53(11):993-1000. [CrossRef]
13. Fischbach F, Porsch M, Krenzien F, et al. MR imaging guided percutaneous nephrostomy using a 1.0 Tesla open MR scanner. *Cardiovasc Intervent Radiol*. 2011;34(4):857-863. [CrossRef]
14. Fischbach F, Wien L, Krueger S, et al. Feasibility study of MR-guided transgluteal targeted in-bore biopsy for suspicious lesions of the prostate at 3 Tesla using a freehand approach. *Eur Radiol*. 2018;28(6):2690-2699. [CrossRef]
15. Gossmann A, Bangard C, Warm M, Schmutzler RK, Mallmann P, Lackner KJ. Real-time MR-guided wire localization of breast lesions by using an open 1.0-T imager: initial experience. *Radiology*. 2008;247:535-542. [CrossRef]
16. Neri E, Bali MA, Ba-Ssalamah A, et al. ESGAR consensus statement on liver MR imaging and clinical use of liver-specific contrast agents. *Eur Radiol*. 2016;26(4):921-931. [CrossRef]
17. Rempp H, Loh H, Hoffmann R, et al. Liver lesion conspicuity during real-time MR-guided radiofrequency applicator placement using spoiled gradient echo and balanced steady-state free precession imaging. *J Magn Reson Imaging*. 2014;40(2):432-439. [CrossRef]
18. Yutzy SR, Duerk JL. Pulse sequences and system interfaces for interventional and real-time MRI. *J Magn Reson Imaging*. 2008;27:267-275. [CrossRef]
19. Richard HM, McMillan A, Staats PN, d'Othee BJ. Real-time MR imaging guidance for percutaneous core biopsy of US- and

CT-negative lesion. *J Vasc Interv Radiol*. 2012;23(11):1539-1542. [CrossRef]

20. Dietrich O, Raya JG, Reeder SB, Reiser MF, Schoenberg SO. Measurement of signal-to-noise ratios in MR images: influence of multichannel coils, parallel imaging, and reconstruction filters. *J Magn Reson Imaging*. 2007;26(2):375-385. [CrossRef]
21. Dietrich O, Raya JG, Reeder SB, Ingrisch M, Reiser MF, Schoenberg SO. Influence of multichannel combination, parallel imaging and other reconstruction techniques on MRI noise characteristics. *Magn Reson Imaging*. 2008;26(6):754-762.
22. Zech CJ, Herrmann KA, Reiser MF, Schoenberg SO. MR imaging in patients with suspected liver metastases: value of liver-specific contrast agent Gd-EOB-DTPA. *Magn Reson Med Sci*. 2007;6(1):43-52. [CrossRef]
23. Bashir MR, Merkle EM. Improved liver lesion conspicuity by increasing the flip angle during hepatocyte phase MR imaging. *Eur Radiol*. 2011;21(2):291-294. [CrossRef]
24. Ernst RR, Anderson WA. Application of fourier transform spectroscopy to magnetic resonance. *Review of Scientific Instruments*. 1966;37:93. [CrossRef]
25. Nagle SK, Busse RF, Brau AC, et al. High resolution navigated three-dimensional T_1-weighted hepatobiliary MRI using gadoxetic acid optimized for 1.5 Tesla. *J Magn Reson Imaging*. 2012;36(4):890-899. [CrossRef]
26. Epstein FH, Mugler JP, Brookeman JR. Spoiling of transverse magnetization in gradient-echo (GRE) imaging during the approach to steady state. *Magn Reson Med*. 1996;35(2):237-245. [CrossRef]
27. Frahm C, Gehl HB, Melchert UH, Weiss HD. Visualization of magnetic resonance-compatible needles at 1.5 and 0.2 Tesla. *Cardiovasc Intervent Radiol*. 1996;19(5):335-340. [CrossRef]
28. Ogura A, Maeda F, Miyai A, Kikumoto R. Effects of slice thickness and matrix size on MRI for signal detection. *Nihon Hoshasen Gijutsu Gakkai Zasshi*. 2005;61:1140-1143. [CrossRef]
29. Okada M, Wakayama T, Yada N, et al. Optimal flip angle of Gd-EOB-DTPA-enhanced MRI in patients with hepatocellular carcinoma and liver metastasis. *Abdom Imaging*. 2014;39(4):694-701. [CrossRef]
30. Kim HY, Choi JY, Park CH, et al. Clinical factors predictive of insufficient liver enhancement on the hepatocyte-phase of Gd-EOB-DTPA-enhanced magnetic resonance imaging in patients with liver cirrhosis. *J Gastroenterol*. 2013;48(10):1180-1187. [CrossRef]
31. Xiao YD, Ma C, Liu J, Li HB, Zhang ZS, Zhou SK. Evaluation of hypointense liver lesions during hepatobiliary phase MR imaging in normal and cirrhotic livers: is increasing flip angle reliable? *Sci Rep*. 2016;6:18942. [CrossRef]